IEEE Access
Multidisciplinary ⋮ Rapid Review ⋮ Open Access Journal

Received 15 December 2022, accepted 28 December 2022, date of publication 30 December 2022,
date of current version 23 January 2023.

Digital Object Identifier 10.1109/ACCESS.2022.3233386

RESEARCH ARTICLE

Analysis and Modeling of Axial Leakage for Spoke-Type Hybrid Permanent Magnet Machines

CHANG-HOON SEOK[1], SEUNG-YOUNG YOON[1,3], HONG-SOON CHOI[1,2], HO-YOUNG LEE[3], AND JANGHO SEO[4]

[1]School of Electronic and Electrical Engineering, Kyungpook National University, Daegu 41566, South Korea
[2]Department of Electrical Engineering, Kyungpook National University, Daegu 41566, South Korea
[3]Advanced Mechatronics Research and Development Group, Korea Institute of Industrial Technology, Daegu 31056, South Korea
[4]School of Automotive Engineering, Kyungpook National University, Sangju 37224, South Korea

Corresponding author: Jangho Seo (j.seo@knu.ac.kr)

This work was supported in part by the BK21 FOUR Project funded by the Ministry of Education, South Korea, under Grant 4199990113966; in part by the Ministry of Trade, Industry and Energy, in 2021, under Grant 20016807; and in part by the Korea Evaluation Institute of Industrial Technology (KEIT).

ABSTRACT In this study, we propose a novel analysis method for a spoke-type permanent magnet (PM) synchronous motor (PMSM) using two types of PMs that consider axial leakage flux using a magnetic equivalent circuit (MEC). Spoke-type ferrite PMSM have the advantage of concentrating magnetic flux; however owing to the shape in which the PMs are arranged along the radial direction, some magnetic flux leaks in the axial direction, which causes inconsistency between the 2D and 3D finite element analysis (FEA) results. Because 3D FEA requires considerable analysis time, using it in the initial design stage of the motor is inefficient. Therefore, we present a new analytical method combined with MEC to overcome the existing inefficient approach. To obtain analysis results equivalent to 3D FEA, the new residual magnetic flux density considering axial flux leakage was applied to 2D FEA PMs using MEC and 2D FEA. The validity of the proposed method was verified through 3D FEA and experiments conducted on the test models using two magnet types.

INDEX TERMS Axial flux leakage, ferrite permanent magnet motor, hybrid magnet, less-rare-earth motor, lumped magnetic equivalent circuit, spoke-type permanent magnet motor.

I. INTRODUCTION

Recently, as the demand for electric vehicles has increased, the interest in electric motors that can replace existing automobile engines is increasing as well. High torque density, high efficiency, and miniaturization are required because the adequate motor output and efficiency must be obtained within the limited space of an electric vehicle. To satisfy these requirements, IPMSMs using rare-earth permanent magnets are widely used in electric vehicles. However, owing to excessive consumption of rare-earth permanent magnet (PM) materials, prices are rising, and supply chains become unstable owing to monopolies in the market [1], [2]. An effective approach to reducing the consumption of rare-earth PM materials is to replace them with motors that use induction machines (IMs) and non-rare-earth material ferrite. Accordingly, research on spoke-type motors, using ferrite and hybrid permanent magnet motors and two magnet types to reduce dependence on rare-earth PM, is attracting attention [3], [4], [5], [6], [7], [8], [9]. Among the various PM motors, the spoke-type ferrite PM motor has a structure in which two magnets face each other. Therefore, it has gained substantial popularity because it can obtain a magnetic flux concentration effect [10], [11], [12], [13], [14], [15], [16]. These spoke-type ferrite PM motors promote magnetic flux concentration when the cross-sectional area of the surfaces of a pair of magnets that generate magnetic flux is larger than that of the air-gap. Therefore, it uses a considerable number of PMs in the limited space of the rotor, which allows for using low-grade PM materials. Therefore, it is a competitive

The associate editor coordinating the review of this manuscript and approving it for publication was Paolo Giangrande.

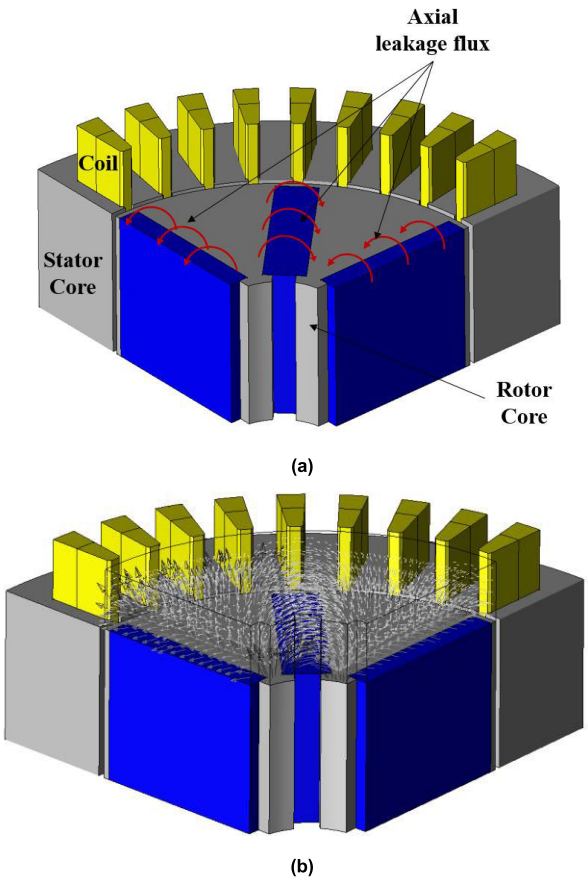

FIGURE 1. Axial magnetic path in spoke-type PMSM. (a) Theoretically estimated axial magnetic path, (b) Axial magnetic path results obtained from 3D FEA.

model because it can replace expensive rare-earth PM motors. However, spoke-type PM motors use many PMs in a limited space, and some magnetic flux leaks in the axial direction because the PMs are arranged along the radial direction. Fig. 1 shows the axial magnetic path obtained through 3D FEA of the spoke-type PM motor. It can be observed that the magnetic flux leaks in the axial direction of the rotor core into which the PM is inserted. The 2D FEA results and experimental data do not match because of the decrease in the back electromotive force (EMF) and torque owing to the axial magnetic flux leakage. Therefore, when designing a spoke-type PM motor, it is necessary to consider the leakage flux in the axial direction using a three-dimensional analysis model. However, 3D FEA considers axial leakage, but it is inefficient in the initial motor design stage because it requires considerable time for analysis. The proposed method uses a novel 2D analysis method that effectively considers axial magnetic flux leakage using 2D FEA and magnetic equivalent circuit (MEC). Using the magnetic properties of the 2D and 3D FEA models, the residual magnetic flux density of the PM was redefined and applied to the proposed 2D FEA. To verify the proposed method, the simulation results obtained from 2D and 3D FEA were compared and analyzed. Finally, the designed motor was built and tested.

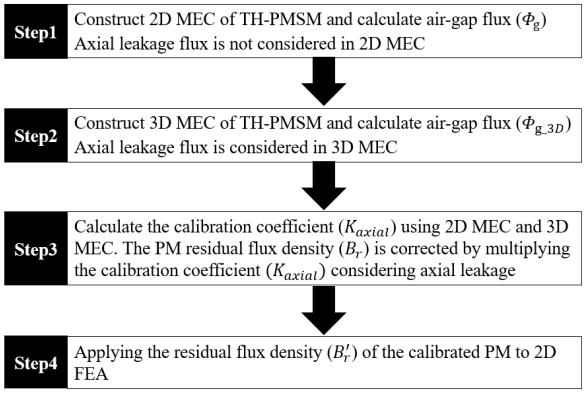

FIGURE 2. Proposed procedure for considering axial leakage magnetic flux of TH-PMSM using 2D FEA.

II. PROPOSED MAGNETIC EQUIVALENT CIRCUITC FOR A TILTED SPOKE-TYPE HYBRID PERMANENT MAGNET SYNCHRONOUS MOTOR

In general, axial leakage flux is not considered in 2D FEA. 3D FEA can consider the axial leakage flux, but it requires substantial computational time. The method and procedure proposed in this study to solve this problem are shown in Fig. 2. This process consists of a total of 4 steps. By constructing 2D and 3D MECs, the pore magnetic flux density of PM at no load was calculated. Calculate the calibration coefficient (K_{axial}) using 2D MEC and 3D MEC. The PM residual magnetic flux density (B_r) is corrected by multiplying the calibration coefficient (K_{axial}) considering axial leakage. The calibration coefficient is applied to the residual magnetic flux density of the two types of permanent magnets. Through this process, the new residual magnetic flux density (B_r') considering the leakage flux in the axial direction is reflected in the 2D FEA, and the result is similar to that of the 3D FEA. To verify the proposed analysis method, a tilted spoke-type hybrid permanent magnet synchronous motor (TH-PMSM) model with a 36/8 slot-pole was used. This model was designed based on a spoke-type motor using two types of PM—rare-earth PM and Ferrite PM—to reduce the consumption of rare-earth PM materials [17].

A. 2D MEC WITHOUT CONSIDERING AXIAL LEAKAGE FLUX

Fig. 3 shows a TH-PMSM machine with a multi-segment permanent magnet composed of Ferrite $PM1$ and rare-earth $PM2$. The magnetic flux generated by the two types of permanent magnets passes through the rotor core, air-gap and stator core; then, it returns to the PM. At this time, some magnetic flux leaked through the bridge. This clearly demonstrates that the air-gap flux can be divided into two parts according to the ratio of $PM1$ to $PM2$. Fig. 4 is the air-gap flux density distribution. The actual curve 1 is simplified like curve 2. N_p is the number of magnet poles and α_p is the pole-arc to pole-pitch ratio. r_i is the radius of the inner diameter of the motor stator, g is the air-gap length between the rotor and stator, and L_{st} is the axial length. Figs. 5 and 6 show the MEC,

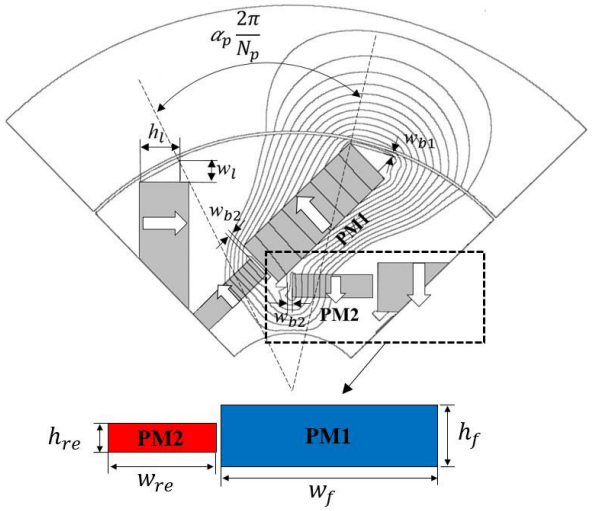

FIGURE 3. TH-PMSM machine structure with two permanent magnet types.

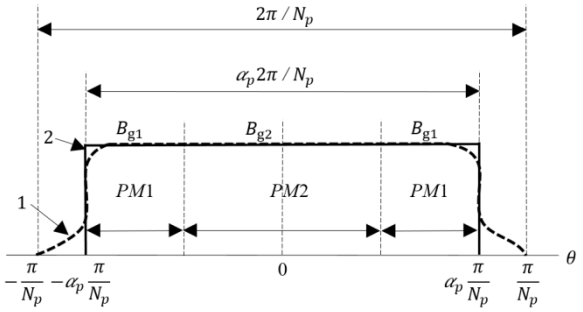

FIGURE 4. Equivalent air-gap flux density distribution.

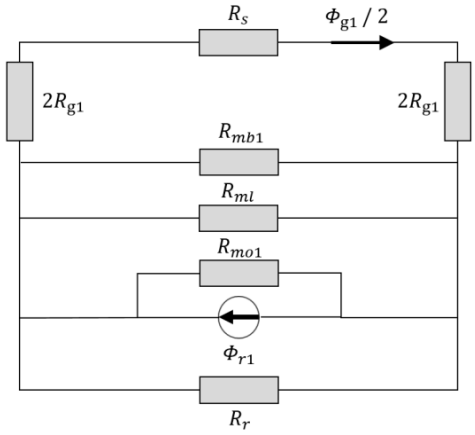

FIGURE 5. 2D MEC model for PM1 in Fig. 2.

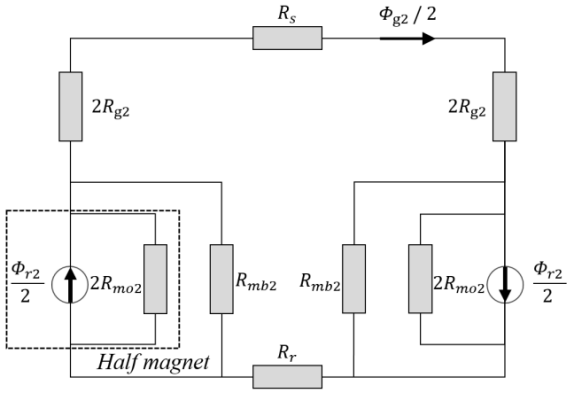

FIGURE 6. 2D MEC model for PM2 in Fig. 2.

including the magnetic flux generated by $PM1$ and $PM2$. Φ_{r1} is the magnetic flux source from $PM1$ and Φ_{r2} is from the $PM2$. Φ_{mo1} and Φ_{mo2} are the magnetic leakage fluxes of $PM1$ and $PM2$, respectively, and the corresponding leakage magnetic resistance values are R_{mo1} and R_{mo2}, respectively. ϕ_{g1} and ϕ_{g2} are the air-gap fluxes, and the corresponding reluctances are R_{g1} and R_{g2}, respectively. Φ_{ml} is the magnetic flux leakage at the end of the magnet and the corresponding magnetic resistance is R_{ml}. R_s and R_r are the stator and rotor core reluctances, respectively. The resistance of air-gap and PM can be expressed by the following equation:

$$R_{mo1} = \frac{h_{m1}}{\mu_0 \mu_r w_{m1} L_{st}} \tag{1}$$

$$R_{mo2} = \frac{h_{m2}}{\mu_0 \mu_r w_{m2} L_{st}} \tag{2}$$

$$A_g = \alpha_p \frac{2\pi\ (r_i - g/2)}{N_p} L_{st} \tag{3}$$

$$R_{g1} = \frac{g}{\mu_0 A_{g1}} \tag{4}$$

$$R_{g2} = \frac{g}{\mu_0 A_{g2}} \tag{5}$$

$$R_{ml} = \frac{2h_l}{\mu_0 w_l L_{st}} \tag{6}$$

where μ_0 denotes the permeability of air; μ_r is the relative permeability of the magnet; and B_{r1} and B_{r2} are the residual magnetic fluxes of $PM1$ and $PM2$. h_{m1} and h_{m2} are the $PM1$ and $PM2$ heights, respectively, and w_{m1} and w_{m2} are the magnet widths. A_{g1} and A_{g2} are the areas of the air-gap through which the magnetic fluxes of $PM1$ and $PM2$ pass, respectively. The leakage flux Φ_{mb} through the bridge can be approximated using the following equation:

$$\Phi_{mb} \approx B_{sat} A_b \tag{7}$$

where $A_b = w_b L_{st}$ is the cross-sectional area of the bridge and b is the bridge width. As the bridge is completely saturated, even under no load, the saturation magnetic flux density B_{sat} for modeling is set to 2.0 [T]. Fig. 7 shows a simplified representation of the equivalent circuit shown in Fig. 5. In general, the magnetic permeability of the rotor and stator core is considerable compared to the air-gap; therefore, the magnetic resistance of the iron core is small, so it can be omitted from the entire magnetic circuit. Therefore, R_s and R_r can be ignored compared with R_g [18], [19], [20]. Using symmetry, Fig. 6 can be represented as a simplified MEC, as shown in Fig. 8. The air-gap flux Φ_{g1} of $PM1$ is expressed as follows:

$$\Phi_{r1} = B_{r1} A_{m1} = B_{r1} w_{m1} L_{st} \tag{8}$$

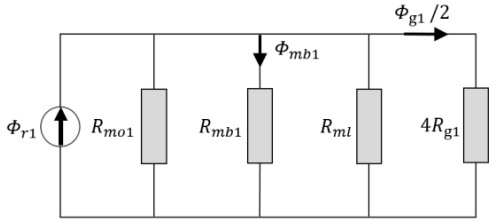

FIGURE 7. Simplified circuit of Fig. 3.

$$\Phi_{g1} = (\Phi_{r1} - \Phi_{mb1})\left(\frac{2R_1}{4R_{g1} + R_1}\right) \tag{9}$$

$$R_1 = R_{mo1} \| R_{ml} \tag{10}$$

Therefore, the air-gap flux density B_{g1} of $PM1$ can be expressed as follows:

$$B_{g1} = \frac{\Phi_{g1}}{A_{g1}} = (\Phi_{r1} - \Phi_{mb1})\left(\frac{2R_1}{4R_{g1} + R_1}\right)/A_{g1} \tag{11}$$

Similarly, according to the circuit shown in Fig. 8, the air-gap flux Φ_{g2} of $PM2$ can be expressed as follows:

$$\Phi_{r2} = B_{r2}A_{m2} = B_{r2}w_{m2}L_{st} \tag{12}$$

$$\Phi_{g2} = (\Phi_{r2} - 2\Phi_{mb2})\left(\frac{R_2}{R_{g2} + R_2}\right) \tag{13}$$

$$R_2 = R_{mo2} \tag{14}$$

Therefore, the air-gap flux density B_{g2} of $PM2$ can be expressed as follows:

$$B_{g2} = \frac{\Phi_{g2}}{A_{g2}} = (\Phi_{r2} - 2\Phi_{mb2})\left(\frac{R_2}{R_{g2} + R_2}\right)/A_{g2} \tag{15}$$

As shown by curve 1 in Fig. 4, which is the actual air gap flux density distribution predicted by FEA, B_{g1} and B_{g2} are very similar. Therefore, for simplicity, they are assumed to be equal, i.e.,

$$B_{g1} \approx B_{g2} \tag{16}$$

Substituting (11) and (15) into (16), the air-gap areas A_{g1} and A_{g2} through which the magnetic fluxes of $PM1$ and $PM2$ pass are derived.

$$\frac{(\Phi_{r1} - \Phi_{mb1})}{A_{g1}}\left(\frac{2R_1}{4R_{g1} + R_1}\right) = \frac{(\Phi_{r2} - 2\Phi_{mb2})}{A_{g2}}\left(\frac{R_2}{R_{g2} + R_2}\right) \tag{17}$$

$$A_{g1} = \frac{\Phi_{r1} - \Phi_{mb1}\left(\frac{1}{R_2} + \frac{1}{R_g}\right) - 2(\Phi_{r2} - 2\Phi_{mb2})\frac{1}{R_1}}{\Phi_{r1} + \frac{1}{2}\Phi_{r2} - \Phi_{mb1} - \Phi_{mb2}}\left(\frac{g}{\mu_0}\right) \tag{18}$$

Fig. 9 compares the air-gap flux density of the previously constructed 2D MEC and 2D FEA. There is a difference in the waveforms at the ends of the poles owing to the fringing effect, but the magnitude of the air-gap flux density is very similar. Consequently, it can be confirmed that a 2D MEC model that reflects the characteristics of the TH-PMSM machine using two types of magnets was developed.

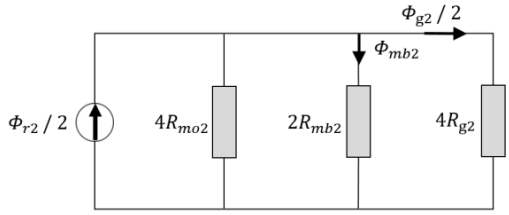

FIGURE 8. Simplified circuit of Fig. 4.

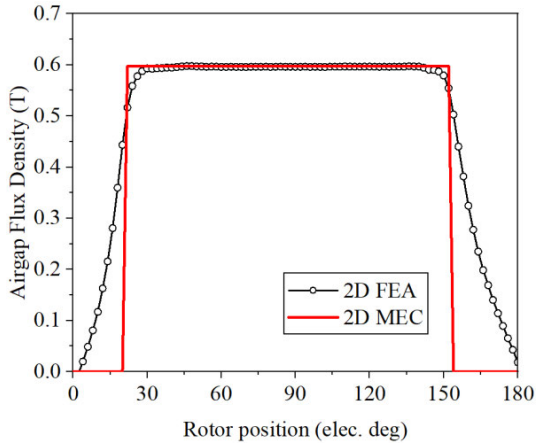

FIGURE 9. Comparison between the air gap flux densities obtained from 2D FEA and MEC.

B. 3D MEC CONSIDERING AXIAL LEAKAGE FLUX

The 3D MEC model adds magnetic resistance corresponding to axial leakage, which cannot be accounted for in 2D MEC. As shown in Fig. 10 (a), the difference between 3D MEC and 2D MEC is the existence of axial leakage flux path. The axial leakage path formed between the rotor cores can be assumed to be semi-circular, as shown in Fig. 10 (b). The magnetic resistance caused by the axial leakage resistance flux can be calculated using the following equations [21], [22], [23], [24], [25], [26]. As $PM1$ and $PM2$ have different magnet types, the magnetic resistance corresponding to axial leakage is expressed as R_{ma_PM1} and R_{ma_PM2}, respectively. R_{ma_PM1} and R_{ma_PM2} are calculated using Eqs. (19)-(21). Fig. 11 shows the 3D MEC, including the magnetic flux generated by $PM1$. The axial leakage resistance, R_{ma_PM1} is added in parallel.

$$R_{ma} = R_{ma1} \| R_{ma2} \tag{19}$$

$$R_{ma1} = \frac{\pi}{\mu_0 2w_m} \tag{20}$$

$$R_{ma2} = \left[\frac{\mu_0 w_m}{\pi} ln\left(1 + \frac{h_f}{h_m}\right)\right]^{-1} \tag{21}$$

The air-gap flux Φ_{g1_3D} of $PM1$ can be expressed as

$$\Phi_{g1\_3D} = (\Phi_{r1} - \Phi_{mb1})\left(\frac{2R_3}{4R_{g1} + R_3}\right) \tag{22}$$

$$R_3 = R_{mo1} \| R_{ml} \| R_{ma\_PM1} \tag{23}$$

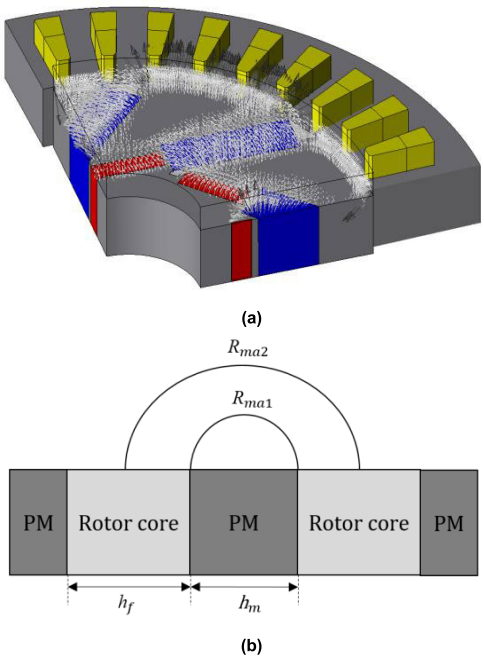

FIGURE 10. Axial leakage flux generated in the rotor core. (a) 3D FEA result of the TH-PMSM, (b) Simplified axial leakage flux path.

Therefore, the air-gap flux density B_{g1_3D} of $PM1$ can be expressed as follows:

$$B_{g1\_3D} = \frac{\Phi_{g1\_3D}}{A_{g1}} = (\Phi_{r1} - \Phi_{mb1}) \left(\frac{2R_3}{4R_{g1} + R_3} \right) / A_{g1} \tag{24}$$

Fig. 12 shows the 3D MEC, including the magnetic flux generated by $PM2$. The axial leakage resistance R_{ma_PM2} was added in parallel. The air-gap flux Φ_{g2} of $PM2$ can be expressed as

$$\Phi_{g2\_3D} = (\Phi_{r2} - 2\Phi_{mb2}) \left(\frac{R_4}{R_{g2} + R_4} \right) \tag{25}$$

$$R_4 = R_{mo2} \| R_{ma\_PM2} \tag{26}$$

$$B_{g2\_3D} = \frac{\Phi_{g2\_3D}}{A_{g2}} = (\Phi_{r2} - 2\Phi_{mb2}) \left(\frac{R_4}{R_{g2} + R_4} \right) / A_{g2} \tag{27}$$

Fig. 13 shows a comparison of the air-gap flux density of the 3D MEC and 3D FEA models. It can be confirmed that the 3D MEC results are very similar to those obtained from the 3D FEA because axial leakage is considered in both.

C. APPLICATION OF CALIBRATION COEFFICIENT CONSIDERING AXIAL LEAKAGE FLUX TO 2D FEA

The air-gap flux density of the 3D model considering the axial leakage is smaller than that of the 2D model. Using the 2D and 3D MEC configured above, the new residual magnetic fluxes of $PM1$ and $PM2$ considering axial leakage can be expressed using the following equation:

$$\Phi_g : \Phi_{g\_3D} = \Phi_{g\_2DFEA} : \Phi_{g\_3DFEA} \tag{28}$$

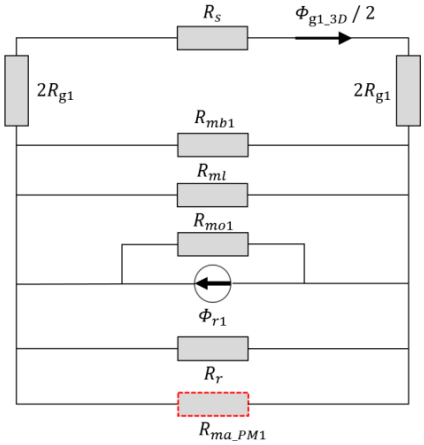

FIGURE 11. 3D MEC model considering the axial leakage flux of PM1.

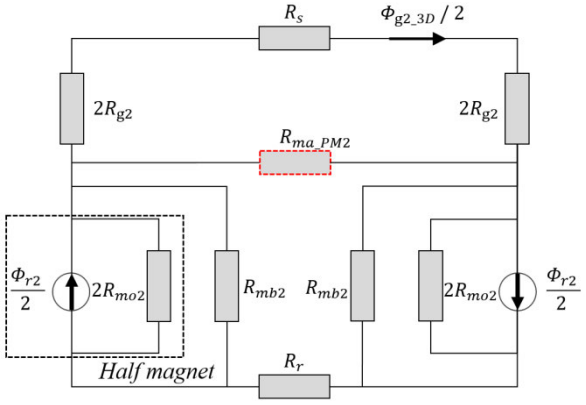

FIGURE 12. 3D MEC model considering the axial leakage flux of PM2.

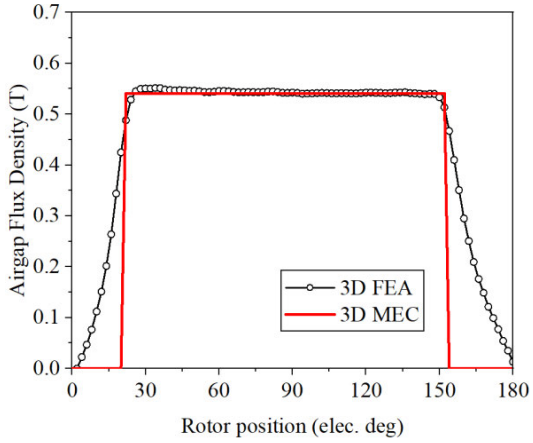

FIGURE 13. Comparison between the air-gap flux densities obtained from 3D FEA and MEC.

$$\Phi_{g\_3DFEA} = \frac{\Phi_{g\_3D}}{\Phi_g} \Phi_{g\_2DFEA} \tag{29}$$

$$K_{axial\_PM1} = \frac{\Phi_{g1\_3D}}{\Phi_{g1}} \tag{30}$$

$$K_{axial\_PM2} = \frac{\Phi_{g2\_3D}}{\Phi_{g2}} \tag{31}$$

$$\Phi_{g1\_3D} = K_{axial\_PM1} \Phi_{g1} = K_{axial\_PM1} (\Phi_{r1} - \Phi_{mb1}) \left(\frac{2R_1}{4R_{g1} + R_1} \right)$$

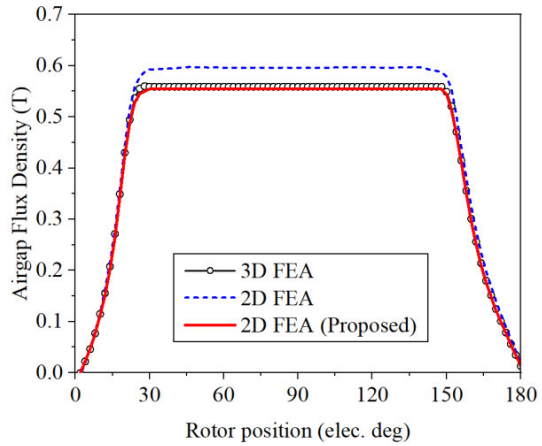

FIGURE 14. Comparison of air-gap flux density of 3D FEA, 2D FEA, and the proposed method.

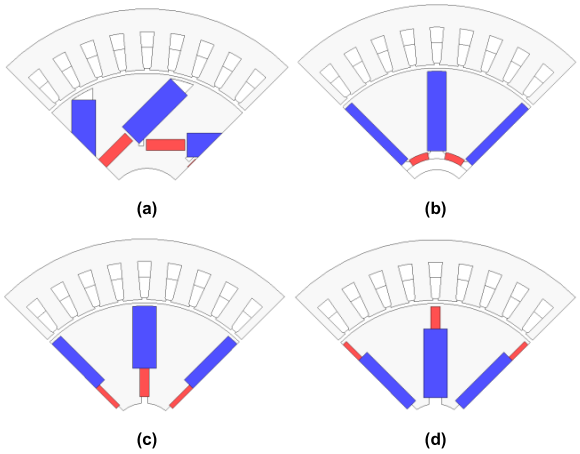

FIGURE 15. Shape of test models. (a) Model-1, (b) Model-2, (c) Model-3, (d) Model-4.

$$= \left(B'_{r1}A_{m1} - B'_{sat1}A_{b1}\right)\left(\frac{2R_1}{4R_{g1}+R_1}\right)$$
$$\left(\because B'_{r1} = K_{axial\_PM1}B_{r1},\ B'_{sat1} = K_{axial\_PM1}B_{sat1}\right) \quad (32)$$

$$\Phi_{g2\_3D} = K_{axial\_PM2}\Phi_{g2}$$
$$= K_{axial\_PM2}\left(\Phi_{r2} - 2\Phi_{mb2}\right)\left(\frac{R_2}{R_{g2}+R_2}\right)$$
$$= \left(B'_{r2}A_{m2} - 2B'_{sat2}A_{b2}\right)\left(\frac{R_2}{R_{g2}+R_2}\right)$$
$$\left(\because B'_{r2} = K_{axial\_PM2}B_{r2},\ B'_{sat2} = K_{axial\_PM2}B_{sat2}\right) \quad (33)$$

The new sets B'_{r1} and B'_{r2} are the new residual magnetic flux densities of $PM1$ and $PM2$, which reflect the 2D and 3D shape coefficients, respectively. Equations (30) and (31) are used to determine the 2D and 3D shape factors for the $PM1$ and $PM2$. Finally, Equations (32) and (33) are used for calculating the new residual magnetic flux densities of $PM1$ and $PM2$. B'_r is smaller than B_r since axial leakage is considered. Fig. 14 shows the analysis results obtained using 3D FEA, 2D FEA, and the proposed method. The proposed method yielded the same results as the 3D FEA analysis.

TABLE 1. Design parameters and dimensions of the test models.

Parameter	Model-1	Model-2	Model-3	Model-4
Poles/Slots		8/36		
Outer diameter (mm)		124		
Air-gap length (mm)		1		
Rated current (A_{peak})		20		
Rated speed (rpm)		1000		
B_{r1} (T)		0.45		
B_{r2} (T)		1.26		
Stack length (mm)		20,30,40		
h_f (mm)	7.5	7.5	7.5	7.5
w_f (mm)	21.3	28.5	19.5	21.6
h_{re} (mm)	3.5	2.2	3	3
w_{re} (mm)	12	5.5	9	7

TABLE 2. Calculated residual flux density and equivalent ratio of the test models.

Analysis model	L_{st} (mm)	B'_{r1} (T)	B'_{r2} (T)	K_{axial_PM1}	K_{axial_PM2}
Model-1	20	0.396	1.216	0.879	0.973
	30	0.422	1.228	0.916	0.982
	40	0.421	1.238	0.936	0.987
Model-2	20	0.404	1.206	0.898	0.965
	30	0.419	1.222	0.930	0.977
	40	0.423	1.228	0.946	0.982
Model-3	20	0.394	1.185	0.876	0.948
	30	0.411	1.206	0.914	0.965
	40	0.420	1.216	0.933	0.973
Model-4	20	0.392	1.195	0.871	0.956
	30	0.410	1.213	0.910	0.970
	40	0.419	1.221	0.931	0.977

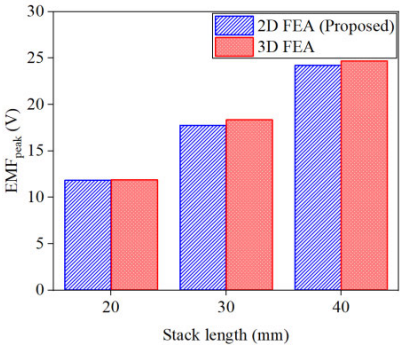

FIGURE 16. Comparison of EMF peak value with respect to the stack length for Model-1.

III. SIMULATION RESULTS

To verify the validity and accuracy of the proposed method, four models with different rotor shapes were selected. Fig. 15 and Table 1 show the shapes and specifications of the four selected models. The MEC was constructed using the circuits shown in Figs. 11 and 12. Table 2 shows the new residual magnetic flux densities B'_{r1} and B'_{r2} of $PM1$ and $PM2$, respectively, in each model. The new residual magnetic flux density considering the axial leakage was observed to be lower than the residual magnetic flux density before correction. As the stack length decreased, the ratio of the axial leakage flux to the total magnetic flux increased. Therefore,

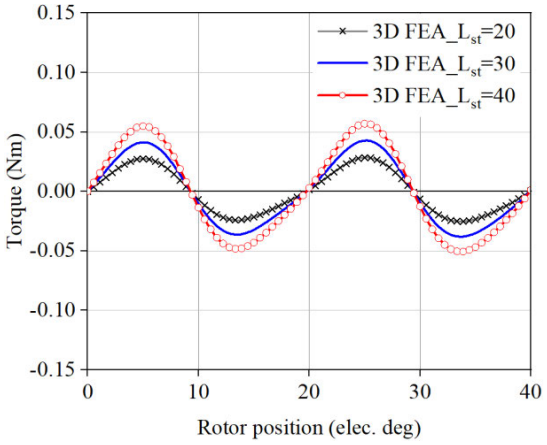

(a)

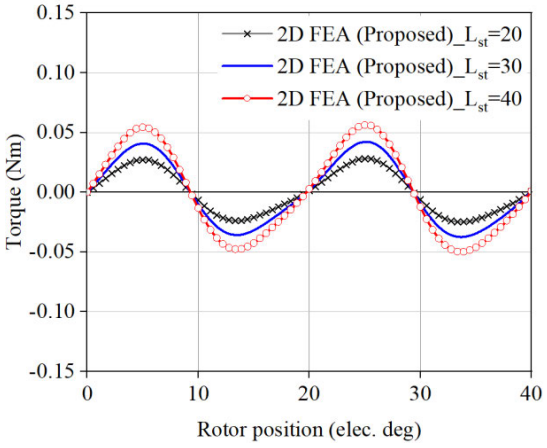

(b)

FIGURE 17. Cogging torque waveform using stack length for Model-1. (a) 3D FEA and (b) proposed.

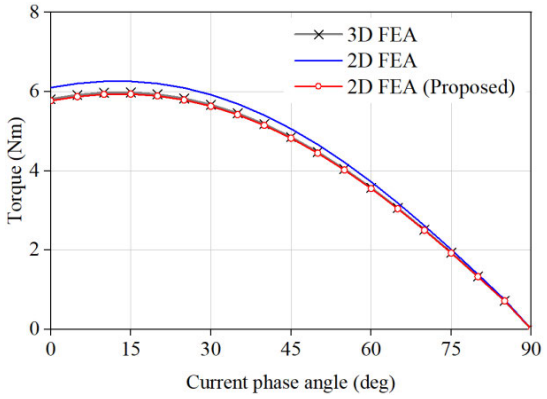

FIGURE 18. Comparison of the output torque versus current angle for Model-1 with L_{st} = 30 mm.

it was confirmed that the B_r' of the permanent magnet gradually decreased as the stacked length decreased. If the ferrite magnet is arranged long in the radial direction, more axial leakage occurs. In addition, as in Model-2, it was confirmed that axial leakage was less when the rare-earth PM was arranged horizontally. Therefore, a motor that uses these two types of magnets requires proper placement. Corrected

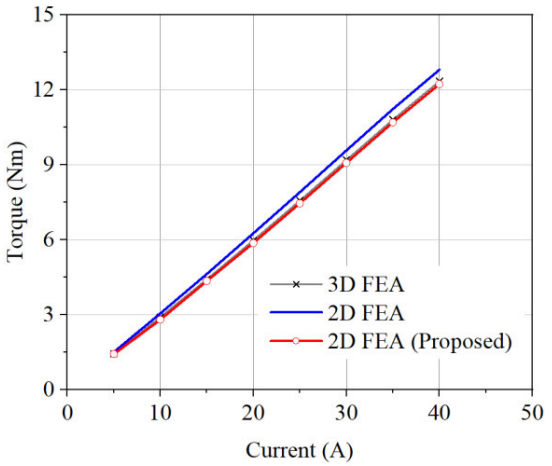

FIGURE 19. Comparison of the output torque versus current amplitude for Model-1 with L_{st} = 30 mm.

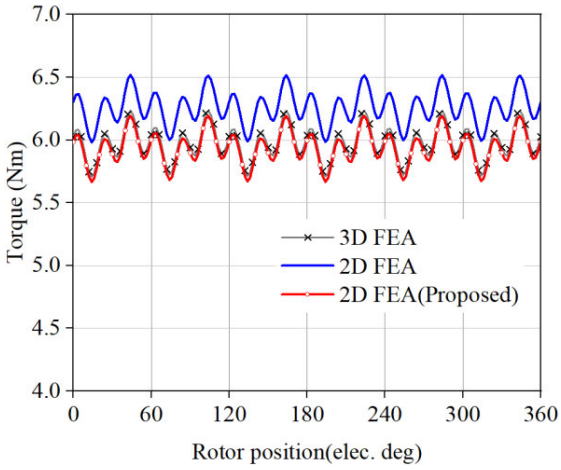

FIGURE 20. Comparison of torque-ripple waveforms for Model-1 with L_{st} = 30 mm under I_{peak} = 20 A.

residual magnetic flux density was applied to the proposed 2D FEA and compared with 3D FEA. Fig. 16 shows the back-EMF waveform of Model-1. The back-EMF waveform obtained by the proposed method was confirmed to be similar to that obtained by 3D FEA. The error between the proposed method and 3D FEA was approximately 1%, whereas that between the 2D FEA and 3D FEA was 6.8%. The back-EMF comparison results for all analytical models are summarized in Table 3. Fig. 17 shows the cogging torque for each method. It can be observed that the torque of the proposed method was considerably different from that of 2D FEA but very similar to that of 3D FEA. Fig. 18 shows the torque curve according to the current angle (β) of Model-1. As a result of the analysis, the maximum torque was observed at current angle β= 15°. A comparison of the average torques using the current amplitude is shown in Fig. 19. When the d-axis current was 15 (β = 15°), even if the magnitude of the current increased, the 3D FEM and proposed method were similar, but the difference from the 2D FEA increased. The results of the proposed method agree well with those of the 3D FEM but not with

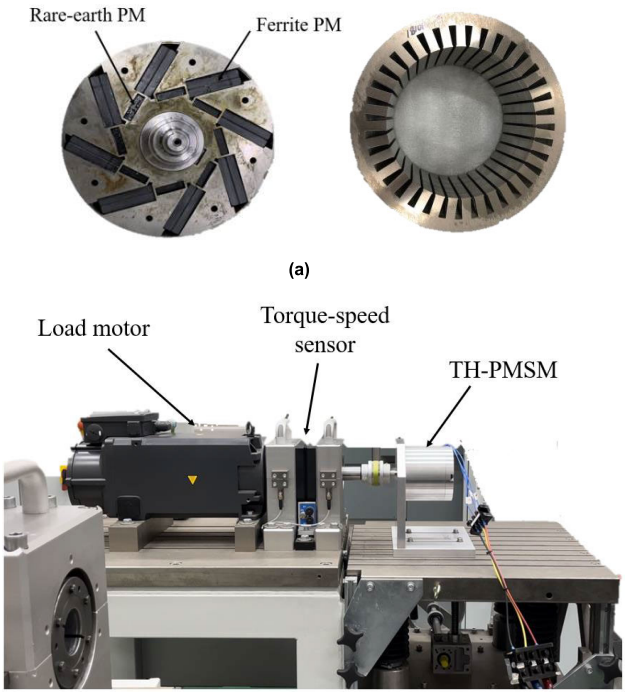

FIGURE 21. Components of TH-PMSM machines. (a) Rotor and stator of the TH-PMSM, (b) Experimental platform.

TABLE 3. Back EMF simulation results of 3D FEM and the proposed method.

Analysis model	L_{st} (mm)	3D FEM (V)	Proposed (V)	Diff (%)
Model-1	20	11.89	11.73	1.3
	30	18.35	18.09	1.4
	40	24.69	24.37	1.3
Model-2	20	9.89	9.75	1.1
	30	17.56	17.33	1.3
	40	20.57	20.31	1.3
Model-3	20	12.13	11.97	1.3
	30	18.64	18.40	1.3
	40	25.17	24.90	1.1
Model-4	20	11.17	11.03	1.2
	30	17.16	16.97	1.1
	40	23.18	22.93	1.1

Diff: Difference = (3D FEA- Proposed)/3D FEA × 100

those of the 2D FEM. The comparison results for the torque ripple are shown in Fig. 20. The errors of the 2D FEA and 3D FEA were 6.2%, and the errors of the proposed method and 3D FEM were 1.1%. To experimentally verify the proposed method, a prototype motor was manufactured with the shape and specifications of Model-1, and it is as shown in Fig. 21. Fig. 22 shows the experimentally measured waveforms and no-load back EMF waveforms analyzed using the proposed method. The back EMF values were measured at a rotation speed of 1000 rpm, and the experiments were conducted at an environmental temperature of 20 °C. According to the no-load back EMF comparison results, the magnitude of error in the effective value was approximately 2%. Accordingly, the results of the proposed method agreed well with those obtained from the experimental data.

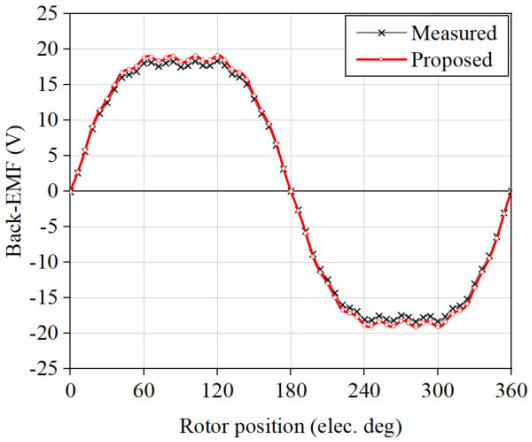

FIGURE 22. Comparison of back-EMF at 1000 r/min.

IV. CONCLUSION

In this study, a novel analysis method for a spoke-type PMSM using two types of PMs considering the axial leakage flux using an MEC is proposed. A new residual magnetic flux density reflecting the axial leakage flux generated by two types of magnets was determined using an MEC and applied to 2D FEA. Therefore, an analysis that considers axial leakage can be performed quickly using proposed method instead of 3D FEA. By verifying the validity of the proposed method under various conditions using 2D and 3D FEA, our proposed method can accelerate the spoke-type PMSM analysis and initial design process.

REFERENCES

[1] H. Tahanian, M. Aliahmadi, and J. Faiz, "Ferrite permanent magnets in electrical machines: Opportunities and challenges of a non-rare-earth alternative," *IEEE Trans. Magn.*, vol. 56, no. 3, pp. 1–20, Mar. 2020.

[2] X. Zhu, L. Wang, Y. Chen, L. Chen, and L. Quan, "A non-rare-earth doubly salient flux controllable motor capable of fault-tolerant control," *IEEE Trans. Magn.*, vol. 51, no. 11, pp. 1–4, Nov. 2015.

[3] Y.-H. Hwang and J. Lee, "HEV motor comparison of IPMSM with Nd sintered magnet and heavy rare-earth free injection magnet in the same size," *IEEE Trans. Appl. Supercond.*, vol. 28, no. 3, pp. 1–5, Apr. 2018.

[4] Q. Chen, G. Liu, W. Zhao, M. Shao, and Z. Liu, "Design and analysis of the new high-reliability motors with hybrid permanent magnet material," *IEEE Trans. Magn.*, vol. 50, no. 12, pp. 1–10, Dec. 2014.

[5] W. Wu, X. Zhu, L. Quan, D. Fan, and Z. Xiang, "Characteristic analysis of a less-rare-earth hybrid PM-assisted synchronous reluctance motor for EVs application," *AIP Adv.*, vol. 7, no. 5, May 2017, Art. no. 056648.

[6] X. Zhu, W. Wu, L. Quan, Z. Xiang, and W. Gu, "Design and multi-objective stratified optimization of a less-rare-earth hybrid permanent magnets motor with high torque density and low cost," *IEEE Trans. Energy Convers.*, vol. 34, no. 3, pp. 1178–1189, Sep. 2019.

[7] Y. Chen, T. Cai, X. Zhu, D. Fan, and Q. Wang, "Analysis and design of a new type of less-rare-earth hybrid-magnet motor with different rotor topologies," *IEEE Trans. Appl. Supercond.*, vol. 30, no. 4, pp. 1–6, Jun. 2020.

[8] Z. S. Du and T. A. Lipo, "Cost-effective high torque density bi-magnet machines utilizing rare earth and ferrite permanent magnets," *IEEE Trans. Energy Convers.*, vol. 35, no. 3, pp. 1577–1584, Sep. 2020.

[9] W. Wu, X. Zhu, L. Quan, Z. Xiang, D. Fan, and S. Yang, "Performance evaluation of a U-shaped less-rare-earth hybrid permanent magnet assisted synchronous reluctance motor," in *Proc. IEEE Vehicle Power Propuls. Conf. (VPPC)*, Oct. 2016, pp. 1–6.

[10] M. Barcaro and N. Bianchi, "Interior PM machines using ferrite to replace rare-earth surface PM machines," *IEEE Trans. Ind. Appl.*, vol. 50, no. 2, pp. 979–985, Mar. 2014.

[11] S. Cho, H. Ahn, H. C. Liu, H.-S. Hong, J. Lee, and S.-C. Go, "Analysis of inductance according to the applied current in spoke-type PMSM and suggestion of driving mode," *IEEE Trans. Magn.*, vol. 53, no. 6, pp. 1–4, Jun. 2017.
[12] S. G. Lee, J. Bae, and W.-H. Kim, "A study on the maximum flux linkage and the goodness factor for the spoke-type PMSM," *IEEE Trans. Appl. Supercond.*, vol. 28, no. 3, pp. 1–5, Apr. 2018.
[13] Q. Chen, G. Xu, F. Zhai, and G. Liu, "A novel spoke-type PM motor with auxiliary salient poles for low torque pulsation," *IEEE Trans. Ind. Electron.*, vol. 67, no. 6, pp. 4762–4773, Jun. 2020.
[14] M. Fontana and N. Bianchi, "Design and analysis of normal saliency IPM spoke motor," *IEEE Trans. Ind. Appl.*, vol. 56, no. 4, pp. 3625–3635, Aug. 2020.
[15] Y. Xiao, Z. Q. Zhu, G. W. Jewell, J. Chen, D. Wu, and L. Gong, "A novel spoke-type asymmetric rotor interior permanent magnet machine," *IEEE Trans. Ind. Appl.*, vol. 57, no. 5, pp. 4840–4851, Sep. 2021.
[16] S. G. Lee, J. Bae, and W.-H. Kim, "Design process of spoke-type permanent magnet synchronous motor considering magnetization performance," *IEEE Trans. Appl. Supercond.*, vol. 30, no. 4, pp. 1–6, Jun. 2020.
[17] C. Seok, H. Choi, and J. Seo, "Design and analysis of a novel spoke-type motor to reduce the use of rare-earth magnet materials," *IET Electr. Power Appl.*, vol. 15, no. 11, pp. 1479–1487, Nov. 2021.
[18] E. C. Lovelace, T. M. Jahns, and J. H. Lang, "A saturating lumped-parameter model for an interior PM synchronous machine," *IEEE Trans. Ind. Appl.*, vol. 38, no. 3, pp. 645–650, Jun. 2002.
[19] M. Rahman, T. Little, and G. Slemon, "Analytical models for interior-type permanent magnet synchronous motors," *IEEE Trans. Magn.*, vol. MAG-21, no. 5, pp. 1741–1743, Sep. 1985.
[20] C.-C. Hwang and Y. H. Cho, "Effects of leakage flux on magnetic fields of interior permanent magnet synchronous motors," *IEEE Trans. Magn.*, vol. 37, no. 4, pp. 3021–3024, Jul. 2001.
[21] R. Qu and T. A. Lipo, "Analysis and modeling of air-gap and zigzag leakage fluxes in a surface-mounted permanent-magnet machine," *IEEE Trans. Ind. Appl.*, vol. 40, no. 1, pp. 121–127, Feb. 2004.
[22] D. C. Hanselman, *Brushless Permanent-Magnet Motor Design*. New York, NY, USA: McGraw-Hill, 1994.
[23] L. Zhu, S. Z. Jiang, Z. Q. Zhu, and C. C. Chan, "Analytical modeling of open-circuit air-gap field distributions in multisegment and multilayer interior permanent-magnet machines," *IEEE Trans. Magn.*, vol. 45, no. 8, pp. 3121–3130, Aug. 2009.
[24] J.-M. Seo, I.-S. Jung, H.-K. Jung, and J.-S. Ro, "Analysis of overhang effect for a surface-mounted permanent magnet machine using a lumped magnetic circuit model," *IEEE Trans. Magn.*, vol. 50, no. 5, pp. 1–7, May 2014.
[25] J. Seo and J.-M. Seo, "Analysis of an interior permanent-magnet machines with an axial overhang structure based on lumped magnetic circuit model," *J. Magn.*, vol. 21, no. 1, pp. 94–101, Mar. 2016.
[26] J.-M. Seo, A.-R. Ro, R.-E. Kim, and J. Seo, "Hybrid analysis method considering the axial flux leakage in spoke-type permanent magnet machines," *IEEE Trans. Magn.*, vol. 56, no. 9, pp. 1–6, Sep. 2020.

CHANG-HOON SEOK received the B.S. degree in physical education from Daegu University, Daegu, South Korea, in 2013, and the M.S. degree in electronic and electrical engineering from Kyungpook National University, Daegu, in 2017, where he is currently pursuing the Ph.D. degree. His current research interest includes design of electric machines.

SEUNG-YOUNG YOON received the B.S. degree in electrical engineering from Gyeongsang National University, Jinju, South Korea, in 2020, and the M.S. degree in electronic and electrical engineering from Kyungpook National University, Daegu, South Korea, in 2022, where he is currently pursuing the Ph.D. degree. His current research interests include design and analysis of electric motors and electro-magnetic field analysis.

HONG-SOON CHOI received the B.S., M.S., and Ph.D. degrees in electrical engineering from Seoul National University, Seoul, South Korea, in 1986, 1988, and 2000, respectively. From 1988 to 1994, he was a Senior Research Engineer at Samsung Electro-Mechanics Company. From 1995 to 1997, he was a Senior Researcher at the Korea Electrical Engineering and Science Research Institute. From 1997 to 2003, he was a Co-Founder and the Research Director of KOMOTEK Company, which develops and produces precision motors. From 2003 to 2006, he was a Research Professor at Sungkyunkwan University. Since 2007, he has been a Professor with the School of Electronic and Electrical Engineering, Kyungpook National University. His current research interests include design of electric machines, theory of electro-magnetic force density, and multi-physics of electrics and mechanics.

HO-YOUNG LEE received the B.S. degree in mechanical engineering from Daegu University, Daegu, South Korea, in 2012, and the M.S. degree in automotive engineering from Hanyang University, Seoul, South Korea, in 2014, where he is currently pursuing the Ph.D. degree. He is also a Researcher with the Korea Institute of Industrial Technology, Daegu. His research interests include design and optimization of electric machine, such as automotive application.

JANGHO SEO received the B.S. degree in electrical and electronics engineering from Chung-Ang University, Seoul, South Korea, in 2003, and the Ph.D. degree in electrical engineering from Seoul National University, Seoul, in 2010. From 2010 to 2012, he was a Research Associate at The University of Sheffield. Since 2012, he has been a Professor with the School of Automotive Engineering, Kyungpook National University. His current research interest includes design of electric machines.